JPE 18-3-22

https://doi.org/10.6113/JPE.2018.18.3.879
ISSN(Print): 1598-2092 / ISSN(Online): 2093-4718

Selection of Coupling Factor for Minimum Inductor Current Ripple in Multi-winding Coupled Inductor Used in Bidirectional DC-DC Converters

Taewon Kang* and Yongsug Suh†

†,*Dept. of Electrical Engineering, Smart Grid Research Center, Chonbuk National University, Jeonju, Korea

Abstract

A bidirectional dc–dc converter is used in battery energy storage systems owing to the growing requirements of a charging and discharging mode of battery. The magnetic coupling of output or input inductors in parallel-connected multi modules of a bidirectional dc–dc converter is often utilized to reduce the peak-to-peak ripple size of the inductor current. This study proposes a novel design guideline to achieve minimal ripple size of the inductor current under bidirectional power flow. The newly proposed design guideline of optimized coupling factor is applicable to the buck and boost operation modes of a bidirectional dc–dc converter. Therefore, the coupling factor value of the coupled inductor does not have to be optimized separately for buck and boost operation modes. This new observation is explained using the theoretical model of coupled inductor and confirmed through simulation and experimental test.

Key words: Coupling factor, Coupled inductor, Generalization, Two-phase interleaved dc–dc converter

NOMENCLATURE

V_1, V_2	Inductor voltage
i_1, i_2	Inductor current
N_1, N_2	Number of winding turns
ϕ_{11}	Flux produced by current i_1 and linked with winding 1
ϕ_{12}	Flux produced by current i_2 and linked with winding 1
ϕ_1	Total flux linked with winding 1
ϕ_{L1}	Leakage flux produced by current i_1
λ_{11}	Flux linkage with winding 1 and produced by $i_1(\lambda_{11} = N_1\phi_{11})$
λ_{12}	Flux linkage with winding 1 and produced by $i_2(\lambda_{12} = N_1\phi_{12})$
λ_1	Total flux linkage with winding $1(\lambda_1 = N_1\phi_1)$
L_{11}	Self-inductance between λ_{11} and $i_1(\lambda_{11} = L_{11}i_1)$
L_{12}	Mutual inductance between λ_{12} and $i_2(\lambda_{12} = L_{12}i_2)$
L_{21}	Mutual inductance between λ_{21} and i_1 $(\lambda_{21} = L_{21}i_1)$
L_m	Mutual inductance in symmetrical core structure
L_s	Self-inductance ($L_s = L_{11}$)
L_1	Total inductance in winding 1
k	Coupling factor $k = \frac{L_m}{\sqrt{L_{11}L_{22}}}$

Manuscript received Sep. 9, 2017; accepted Dec. 15, 2017
Recommended for publication by Associate Editor Il-Oun Lee.
†Corresponding Author: ysuh@jbnu.ac.kr
Tel: +82-63-270-3381, Chonbuk National University
*Dept. Electr. Eng., Smart Grid Res. Center, Chonbuk Nat'l Univ., Korea

I. INTRODUCTION

Battery energy storage system (BESS) is widely accepted in many industrial application fields. Distributed power generation and micro-grid applications that utilize renewable energy sources are actively adopting BESS to enhance the availability, reliability, and efficiency of the total system. In general, BESS involves a bidirectional power flow to cope with the charging and discharging operations of a battery. A bidirectional dc–dc converter can be utilized to implement this bidirectional power flow in the power conditioning system of the BESS [1]-[6]. Bidirectional dc–dc converters in BESS involve many functional requirements. For example, the requirement of low THD and small ripple for charging–discharging current plays a significant role in determining the

© 2018 KIPE

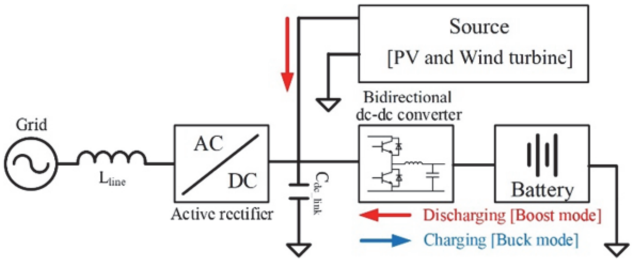

Fig. 1. Block diagram of the BESS-based battery charging system.

life cycle and reliability of battery. This requirement can be achieved by various power electronic techniques. Phase-staggering operation of multiple bidirectional dc–dc converters in parallel connection is considered to reduce the ripple size of summed inductor currents and mitigate the filtering requirement for the battery charging current. A reduction in inductor current ripple by a coupled inductor in the interleaving structure of multiple bidirectional dc–dc converter has also been proposed [9]-[11].

A coupled inductor can decrease the physical size of the inductor while still complying with the peak switching current limitation of power semiconductor switches in dc–dc converters. Design and analysis on two or multi-winding coupled inductors under the phase-staggering operation of multiple dc–dc converters have been reported in previous literature, as summarized in Table I.

The coupling factor of a coupled inductor significantly impacts the phase-staggering operation of multiple bidirectional dc–dc converters and the flux distribution within the inductor core. Therefore, the selection of the optimal magnetic structure and coupling factor is an important task in designing a coupled inductor. The optimal coupling factor and magnetic structure of a coupled inductor applied in step-down dc–dc converters under the phase-staggering operation mode have been investigated [12], [13].

However, these previous studies have only focused on the unidirectional power flow mode of dc–dc converters and coupled inductors, i.e., battery charging mode. Bidirectional power flow is an essential feature of bidirectional dc–dc converters in BESS. Thus, the optimal design of coupling factor and magnetic structure of the coupled inductor should be applied in both the step-down mode and the step-up mode operation of a bidirectional dc–dc converter. In other words, the selection of coupling factor and magnetic structure of the coupled inductor should be optimized for bidirectional operation of dc–dc converters. However, the optimal coupling factor of a coupled inductor and its relationship with the operation of bidirectional dc–dc converters have been rarely explored.

This study investigates the optimal design of coupling factor and the magnetic structure of a coupled inductor in bidirectional dc–dc converters applied for BESS. The optimal coupling factor of the coupled inductor is intended to increase

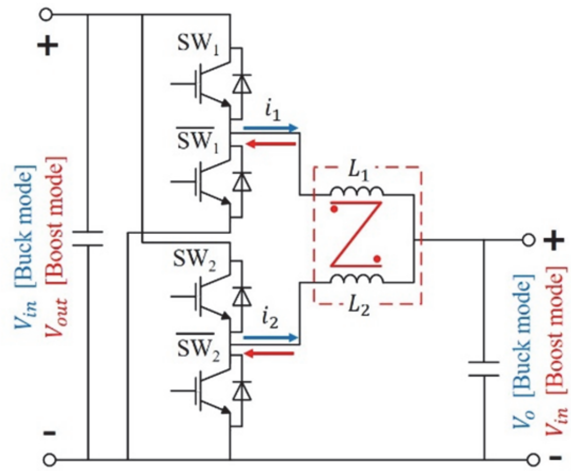

Fig. 2. Bidirectional interleaved dc–dc converter.

the inductor's effective inductance and decrease the peak switching current stress on power semiconductors while keeping the same physical size of the inductor. This study extends the previous work of unidirectional dc–dc converters into bidirectional dc–dc converters [14]-[17], [19]-[22]. The process of selecting the optimal coupling factor is newly presented in consideration of step-down and step-up operations of bidirectional dc–dc converters.

The rest of the paper is structured as follows. Section II describes the overall BESS and bidirectional dc–dc converter considered in this work. Section III explains the analysis and design process for the optimal coupling factor of a coupled inductor with two windings in two-phase parallel-connected bidirectional dc–dc converters under step-down and step-up operation modes. Simulations and experimental verification results are presented in Section IV.

II. DESCRIPTION OF OVERALL SYSTEM

The latest advancement in battery technology has accelerated the acceptance of BESS in many application fields of power system. In general, most battery types used in BESS, including lithium-based batteries, store electrical energy in the form of dc voltage source due to their intrinsic electrochemical characteristics. Therefore, BESS usually requires the power converter system, which converts the dc voltage source from batteries to the ac voltage source, to be connected to a power system of ac frequency. The growing penetration of renewable energy sources, such as photovoltaic and wind turbines, in the power system raises the possibility of intermediate dc grid connection of multiple renewable sources together with BESS. The dc grid connection in a relatively close distance range offers many advantages over the classical ac grid connection, such as unnecessary ac synchronization, simpler droop control, reduction in multiphase cable cost, and elimination of redundant offline ac–dc converters. This concept of intermediate dc grid connection

TABLE I
SUMMARY OF PREVIOUS WORKS ON COUPLED INDUCTOR

	In this paper	[12]	[13]	[14]	[15]	[16]	[17]	[18]
Topology	**Bidirectional dc–dc converter**	Bidirectional dc–dc converter	PFC converter	Boost converter	Three-level dc-dc converter	Buck converter	Boost converter	Bidirectional dc–dc converter
Number of windings	**2**	*n*	2	2	2 and 3	*n*	2	2
Analysis method	**Inductor voltage equation**	Inductor voltage equation	Kirchhoff's law and Faraday's law	IWCI method	Pole voltage equation	Magnetic circuit equation	Inductor voltage equation	Magnetic circuit equation
Design target	**Inductor current ripple**	Transient response, Current ripple	Maximum flux	Maximum flux	Inductor current ripple	Inductor current ripple	Analysis of CCM, DCM	Core design
Coupling factor (k)	**Optimal k under each duty ratio**	0.622 under two windings	0.943	0.946	0.832	0.33	None	0.366

for multiple renewable energy sources and BESS, together with a common offline ac–dc converter has been gaining wide acceptance, particularly in micro-grid systems. This study focuses on the BESS that shares the dc connection network with other renewable sources.

Fig. 1 presents the overall system block diagram of thre target BESS and its dc–dc converter. BESS and multiple renewable energy sources present a common dc grid connection, i.e., dc-link stage. Batteries are connected to a common dc grid through dc–dc converters. BESS involves a bidirectional power flow depending on the charging and discharging modes of batteries. Thus, the dc–dc converter must deal with a bidirectional power flow, which results in a bidirectional dc–dc converter. The typical bidirectional dc–dc converter used in this study is shown in Fig. 2. The topology of the circuit in this figure is classified as two non-isolated half-bridge cells connected in parallel. In general, the intermediate dc-link voltage is higher than the battery voltage. Therefore, the half-bridge cell operates as a step-down converter (buck converter) during the battery charging mode. By contrast, a step-up converter (boost converter) operation is implemented by the half-bridge cell during the battery discharging mode [23], [24].

When multiple dc–dc converter cells are connected in parallel, the switching phase of the semiconductor switch in each cell is usually phase-staggered, i.e., interleaved switching. As a result, the dominant harmonic components of the inductor currents cancel out one another, leading to the summed battery current of less ripple. This reduced ripple of the battery current improves the reliability of the battery and eventually prevents sudden declining of lifetime [25]-[27]. In addition to the interleaved switching operation technique, the coupling of output inductors can also reduce the peak ripple value of inductor current [28], [29]. The coupling of output inductors for multiple half-bridge cells is shown in Fig. 2. In the present study, two windings from each output inductor of half-bridge cell are magnetically cross-coupled. The self-inductance value of this inductor plays a critical role in determining the ripple size of the battery current. Although increasing the value of self-inductance may be a straightforward solution to decrease the ripple size of the battery current, the

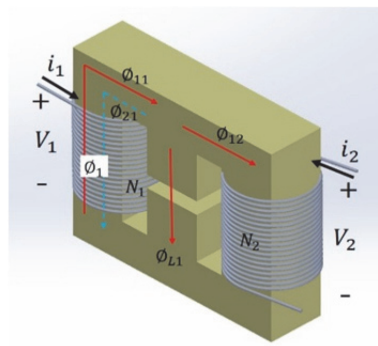

Fig. 3. Magnetic structure of the coupled inductor used in dc–dc converter.

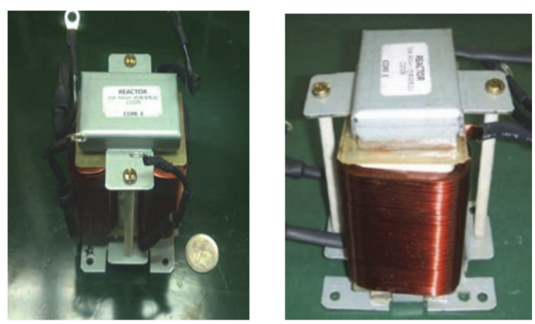

Fig. 4. Photo of the coupled inductor used in the prototype.

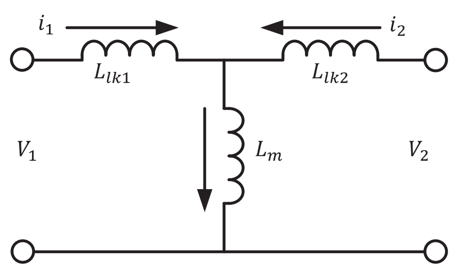

Fig. 5. Equivalent circuit of the coupled inductor.

limitations of cost, weight, and volume profile on the output inductor make this approach impractical. This study proposes a novel way to achieve reduction in the inductor current ripple by applying an optimized coupling factor, not only for the buck operation mode but also for the boost operation mode of the coupled inductor.

III. ANALYSIS AND DESIGN OF COUPLED INDUCTOR

In this section, the analysis and design of the coupled inductor used for two parallel-connected half-bridge cells in Fig. 2 are presented. The coupled inductor equipped with two windings presents a magnetic core structure as shown in Fig. 3. The magnetic core of the coupled inductor is composed of three legs. The center leg exhibits a dominant air gap. Magnetic coupling between two windings can be controlled by varying the length of the air gap in the center leg. The proposed magnetic core structure can provide symmetrical magnetic performance, such as same self-inductance for each winding. A photograph of the coupled inductor with the proposed magnetic core structure is shown in Fig. 4. This coupled inductor is also used in the experimental verification test.

Among the numerous design factors related to a coupled inductor, the coupling factor among multiple windings plays an important role in determining the various characteristics of the coupled inductor, such as the ripple size of the inductor current. An optimized coupling factor that generates the least ripple size of the inductor current under different operating conditions should be introduced. Previous studies on the coupled inductor in dc–dc converters are summarized in Table I. The table shows that no previous works have focused on calculating the optimal coupling factor that generates the least size of inductor ripple current for a bidirectional dc–dc converter. The current study analyzes the operation of the coupled inductor under buck and boost modes of operation. On the basis of this analysis, the optimal value of coupling factor for both operation modes is calculated. Optimized coupling factor for the minimum inductor current ripple is derived on the basis of the equivalent circuit of the coupled inductor in Fig. 5 and the phase-staggering operation of multi paralleled buck converters in Fig. 2. In general, the inductor voltages of the coupled inductor can be represented by the self-inductance and mutual inductance as in (1) and (2). Flux linkage equations are written under the condition of direct coupling for general description.

$$V_1 = \frac{d}{dt}(\lambda_{11} + \lambda_{12}) = L_{11}\frac{d}{dt}i_1 + L_{12}\frac{d}{dt}i_2 \tag{1}$$

$$V_2 = \frac{d}{dt}(\lambda_{22} + \lambda_{21}) = L_{22}\frac{d}{dt}i_2 + L_{21}\frac{d}{dt}i_1 \tag{2}$$

In (1) and (2), L_{11} and L_{22} represent the self-inductance terms, while L_{12} and L_{21} represent the mutual inductance terms. Mutual inductances are equal to each other on the basis of the reciprocity property, as shown in (3).

$$\frac{\lambda_{21}}{i_1} = \frac{\lambda_{12}}{i_2} = L_{21} = L_{12} = L_m \tag{3}$$

Coupling factor (*k*) is the key design factor in a coupled inductor and is defined as in (4). Positive coupling factor refers to a direct coupling, whereas a negative number indicates an inverse coupling. The coupled inductor used in this study adopts the symmetric magnetic structure shown in Fig. 3.

$$k = \frac{L_m}{\sqrt{L_{11}L_{22}}} \tag{4}$$

With the use of (3) and (4), the inductor voltage equations of (1) and (2) can be simplified to (5) [26]. Given the coupling mechanism of the inductor, two inductor voltages (V_1, V_2) are correlated to each other depending on the switching states of SW_1 and SW_2. Four combinations of switching states are possible as explained in Table II [26]. The inductor voltage equation of (5) can be further simplified to (6) and (7) using one of the four equations in Table II and depending on the switching state. In (6) and (7), a variable inductance (L_{eq}) is a function of time, i.e., a function of switching states.

$$V_1 - kV_2 = (1 - k^2)L_{11}\frac{d}{dt}i_1 \tag{5}$$

$$V_1 = L_{eq}\frac{d}{dt}i_1 \tag{6}$$

$$V_2 = L_{eq}\frac{d}{dt}i_2 \tag{7}$$

As a result, the coupled inductor presents a variable equivalent inductance (L_{eq}) depending on the corresponding time interval during switching cycle. This variable equivalent inductance can be either smaller or larger than the self-inductance (L_{11} and L_{22}), depending on the value of the duty ratio (D) and coupling factor (*k*).

A. Buck Converter Mode

In this subsection, the coupled inductor model as described in (6) and (7) is utilized to derive the relationship between the coupling factor and the ripple size of the inductor current under the buck converter operation mode. The total peak-to-peak ripple size of inductor current (i_1) can be represented by several terms, depending on the size of duty as shown in (8) and (9). In (8), the value of Δi_{Lpp_m1} (increment in inductor current i_1 during Mode 1 in Table II) represents the total peak-to-peak ripple of i_1 under the condition D < 0.5, as illustrated in Fig. 6. On the contrary, under the condition of D > 0.5, the total peak-to-peak ripple of i_1 is represented by Δi_{Lpp_m3} (decrement in inductor current i_1 during Mode 3 in Table II). Therefore, the value

TABLE II
EQUIVALENT INDUCTANCE UNDER DIFFERENT SWITCH MODES

Mode	Inductor voltage [Buck Mode]	Inductor voltage [Boost mode]	Correlation of inductor voltages	Equivalent inductance (L_{eq})
Mode 1	$V_1 = V_{in} - V_o$ $V_2 = -V_o$	$V_1 = V_{in}$ $V_2 = V_{in} - V_o$	$V_2 = \frac{-D}{1-D} V_1$	$L_{eq} = \frac{1-k^2}{1+\frac{D}{1-D}k} L_s$
Mode 2	$V_1 = -V_o$ $V_2 = -V_o$	$V_1 = V_{in} - V_o$ $V_2 = V_{in} - V_o$	$V_2 = V_1$	$L_{eq} = (1+k)L_s$
Mode 3	$V_1 = -V_o$ $V_2 = V_{in} - V_o$	$V_2 = V_{in} - V_o$ $V_2 = V_{in}$	$V_2 = \frac{1-D}{-D} V_1$	$L_{eq} = \frac{1-k^2}{1+\frac{1-D}{D}k} L_s$
Mode 4	$V_1 = V_{in} - V_o$ $V_2 = V_{in} - V_o$	$V_1 = V_{in}$ $V_2 = V_{in}$	$V_2 = V_1$	$L_{eq} = (1+k)L_s$

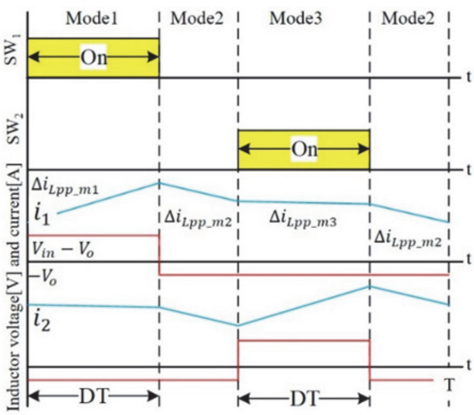

Fig. 6. Voltage mode and inductor current of the two-winding coupled inductor under buck mode and D < 0.5.

of Δi_{Lpp_m1}, which is the increment in inductor current i_1 during Mode 1 in Table II, is calculated as shown in (10). Equation (11) describes the value of Δi_{Lpp_m3}, i.e., the decrement in inductor current i_1 during Mode 3 in Table II. Plugging the corresponding equivalent inductance value (L_{eq}) from Table II into (10) and (11) yields (12) and (13), respectively. In (12) and (13), the total peak-to-peak ripple of i_1 is a function of the coupling factor (k) while keeping the input voltage (V_{in}) and duty (D) constant. The minimum inductor current ripple is obtained when the equivalent inductance is at its maximum. Therefore, the optimal coupling factor of the coupled inductor for the minimal current ripple is to set the equivalent inductance terms in (12) and (13) at its maximum values.

$$\Delta i_{Lpp\_m1} = \Delta i_{Lpp\_m2} + \Delta i_{Lpp\_m3} + \Delta i_{Lpp\_m2} \quad \text{(under D < 0.5)} \tag{8}$$

$$\Delta i_{Lpp\_m3} = \Delta i_{Lpp\_m4} + \Delta i_{Lpp\_m1} + \Delta i_{Lpp\_m4} \quad \text{(under D > 0.5)} \tag{9}$$

$$\Delta i_{Lpp\_m1} = \frac{V_{in} - V_o}{L_{eq}} DT \qquad \text{(under D < 0.5)} \tag{10}$$

$$\Delta i_{Lpp_{m3}} = \frac{V_o}{L_{eq}}(1-D)T \qquad \text{(under D > 0.5)} \tag{11}$$

$$\Delta i_{Lpp\_m1} = \frac{V_{in} DT}{L_s} \frac{1 - D + kD}{1 - k^2} = f(k) \tag{12}$$

$$\Delta i_{Lpp\_m3} = \frac{V_{in}(1-D)T}{L_s} \frac{D + k - kD}{1 - k^2} = f(k) \tag{13}$$

B. Boost Converter Mode

In this subsection, the coupled inductor model as described in (6) and (7) is utilized to derive the relationship between the coupling factor and the ripple size of the inductor current under the boost converter operation mode. In the same manner as in the buck operation mode, the total peak-to-peak ripple size of inductor current (i_1) can be represented by several terms depending on the size of duty as shown in (14) and (15). In (14), the value of Δi_{Lpp_m1} (increment in inductor current i_1 during Mode 1 in Table II) represents the total peak-to-peak ripple of i_1 under the condition D < 0.5, as illustrated in Fig. 7. By contrast, under the condition D > 0.5, the total peak-to-peak ripple of i_1 is represented by Δi_{Lpp_m3} (decrement in inductor current i_1 during Mode 3 in Table II). Therefore, the value of Δi_{Lpp_m1}, which is the increment in inductor current i_1 during Mode 1 in Table II, is calculated as shown in (16). Equation (17) describes the value of Δi_{Lpp_m3}, i.e., the decrement in inductor current i_1 during Mode 3 in Table II. Plugging the corresponding equivalent inductance value (L_{eq}) from Table II into (16) and (17) yields (18) and (19), respectively. In (18) and (19), the total peak-to-peak ripple of i_1 is a function of the coupling factor (k) while keeping the input voltage (V_{in}) and duty (D) constant. Minimum inductor current ripple is obtained when the equivalent inductance is at its maximum. Therefore, the optimal coupling factor of the coupled inductor for the minimal current ripple is to set the equivalent inductance terms in (18) and (19) at its maximum values.

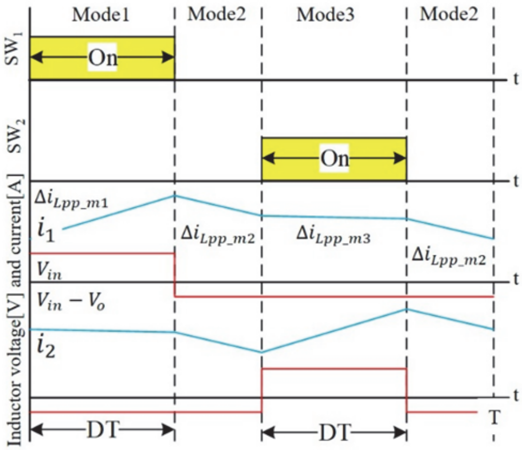

Fig. 7. Voltage mode and inductor current of the two-winding coupled inductor under boost mode and D < 0.5.

$$\Delta i_{Lpp\_m1} = \Delta i_{Lpp\_m2} + \Delta i_{Lpp\_m3} + \Delta i_{Lpp\_m2} \quad \text{(under D < 0.5)} \tag{14}$$

$$\Delta i_{Lpp\_m3} = \Delta i_{Lpp\_m4} + \Delta i_{Lpp\_m1} + \Delta i_{Lpp\_m4} \quad \text{(under D > 0.5)} \tag{15}$$

$$\Delta i_{Lpp\_m1} = \frac{V_{in}}{L_{eq}} DT \quad \text{(under D < 0.5)} \tag{16}$$

$$\Delta i_{Lpp_{m3}} = \frac{V_o - V_{in}}{L_{eq}} (1-D)T \quad \text{(under D > 0.5)} \tag{17}$$

$$\Delta i_{Lpp\_m1} = \frac{V_{in} DT}{L_s (1-D)} \frac{1-D+kD}{1-k^2} = f(k) \tag{18}$$

$$\Delta i_{Lpp\_m3} = \frac{V_{in} T}{L_s} \frac{D+k-kD}{1-k^2} = f(k) \tag{19}$$

$$k_{opt} = \frac{-1+D+\sqrt{1-2D}}{D} \quad (\text{under } D < 0.5) \tag{20}$$

$$k_{opt} = \frac{-D+\sqrt{2D-1}}{1-D} \quad (\text{under } D > 0.5) \tag{21}$$

IV. System Verification

This section presents the simulation and experimental verification results for the proposed mathematical equation of optimal coupling factor in (20) and (21). Simulation and experimental verification are performed with the two-winding coupled inductor in two-phase staggered bidirectional dc–dc converter modules, as shown in Fig. 2. The influence of two-winding coupled inductors with different coupling factors on the ripple size of the inductor current is investigated and compared with that of the theoretical model. The simulation and experiment are carried out for buck and boost operation

TABLE III
Test Specifications for Verification

	Buck mode	Boost mode
Input voltage	300 V	100 V
Self-inductance	1.1 mH	1.1 mH
Coupling factor	−0.3	−0.3
Duty ratio	0.4	0.3
Output Cap.	330 uF	330 uF

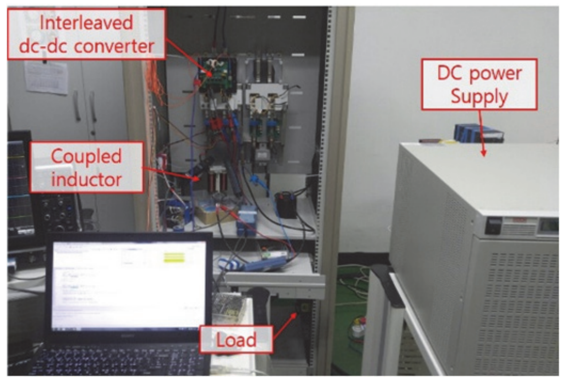

Fig. 8. Hardware test setup for coupled inductor testing.

modes separately. Table III shows the test specification for verification of test and simulation.

The verification process of the experiment requires multiple coupled inductors with different coupling factors. Thus, the experiment is conducted with the help of a hardware-in-the-loop simulation (HILS) setup, particularly for realizing coupled inductors with various coupling factors. In other words, the coupled inductor model available from HILS is used and substituted in place of a real coupled inductor. To verify the validity of this coupled inductor model from HILS, the test result using HILS is compared with the complete hardware test result by using a real coupled inductor of the same coupling factor. In this paper, the test result using the HILS model of coupled inductor and the real coupled inductor with the same coupling factor of 0.3 is presented. Verification of the coupled inductor's HILS model is performed under the buck and boost operation modes.

The complete hardware test setup is illustrated in Fig. 8. The conceptual block diagram explaining the basic application principle of Typhoon HILS is shown in Fig. 9. Fig. 10 describes the test setup employing the coupled inductor model from Typhoon HILS.

A. *Verification of Buck Converter Mode*

In this subsection, the simulation and experimental results for the coupled inductor under buck operation mode is presented. Unless otherwise noted in this paper, the simulation and experimental results under buck operation mode correspond to the duty ratio of 0.4. The simulation and experimental results are likewise compared with a coupling factor of −0.3 (inverse coupling).

Fig. 9. Conceptual block diagram describing the application principle of Typhoon HILS.

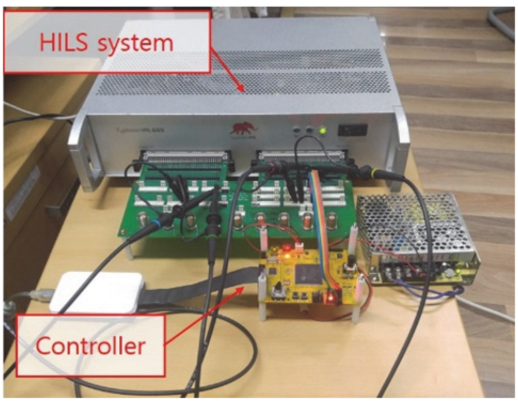

Fig. 10. Test setup of hardware-in-the-loop simulator for coupled inductor testing.

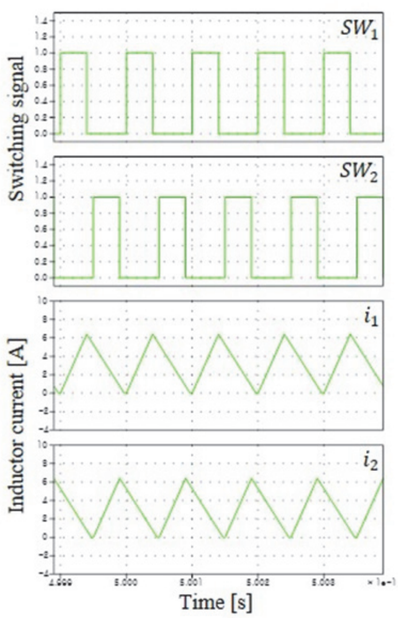

Fig. 11. Simulation waveforms of inductor currents under duty = 0.4 and coupling factor = 0 (non-coupled).

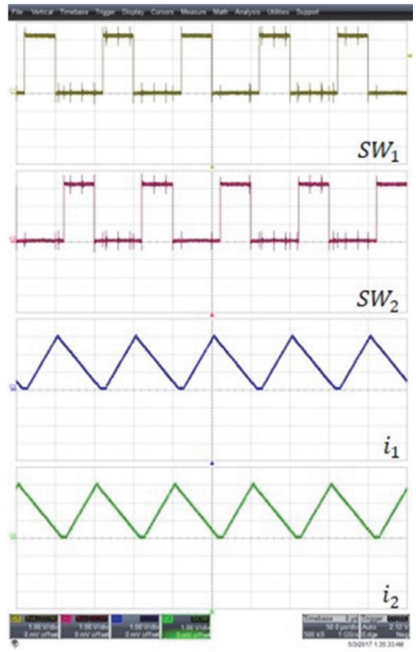

Fig. 12. HILS waveforms of inductor currents under duty = 0.4 and coupling factor = 0 (non-coupled) (i_1, i_2 [2 A/div, 50 us/div]).

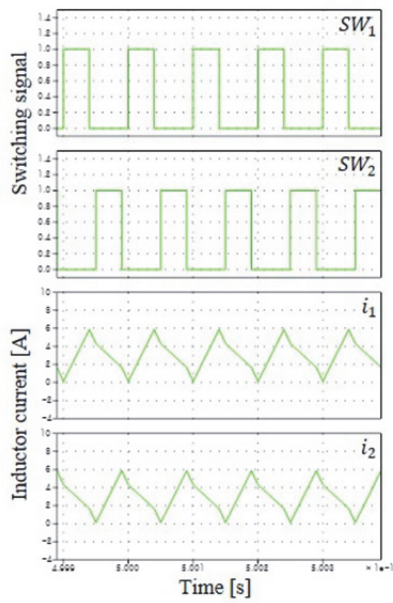

Fig. 13. Simulation waveforms of coupled inductor currents under duty = 0.4 and coupling factor = −0.3.

Waveforms obtained through the simulation and HILS are presented in Figs. 11 and 12, respectively. The waveforms in these figures correspond to the operation condition under which the duty ratio is set to 0.4 and the coupling factor is maintained at 0, i.e., non-coupled. Therefore, these waveforms represent the gate switching signal and the inductor current for the two-phase staggering operation of two buck converter modules with two separate non-coupled inductors. Figs. 13–15 show the simulation, HILS, and experimental waveforms of gate switching signal and the

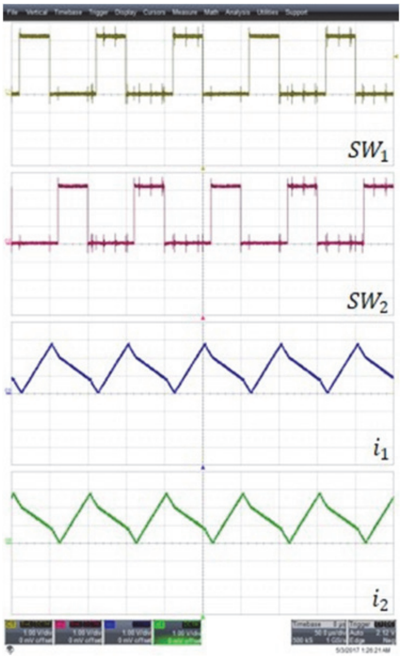

Fig. 14. HILS waveforms of coupled inductor currents under duty = 0.4 and coupling factor = −0.3 (i_1, i_2 [2 A/div, 50 us/div]).

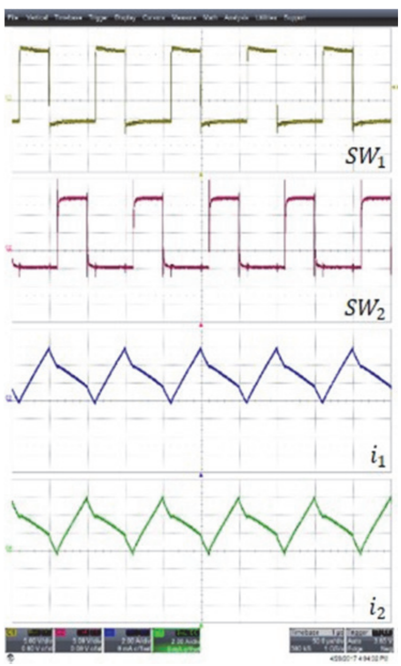

Fig. 15. Experiment waveforms of coupled inductor currents under duty = 0.4 and coupling factor = −0.3 (i_1, i_2 [2 A/div, 50 us/div]).

inductor currents (i_1 and i_2) under the duty of 0.4 and the coupling factor of −0.3 (inverse coupling) in the two phase-staggered operation. An obvious contrast is found between the slope of the inductor current in Figs. 11–12 and in Figs. 13–15. Figs. 13–15 show that the magnetic coupling of output inductors leads to the variation in current slope

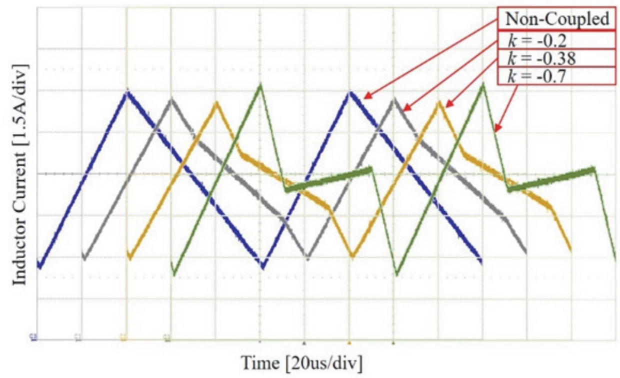

Fig. 16. HIL waveforms of coupled inductor current vs. coupling factor under duty ratio = 0.4.

during the ramping down of inductor currents in the same manner as those in Fig. 6. Fig. 14 represents the waveforms obtained from HILS using the coupled inductor model of Typhoon HILS. The waveforms of inductor current in Fig. 14 are very similar to those in Fig. 15, which were measured from the real experimental setup using the real coupled inductor of the same coupling factor. Therefore, the model of coupled inductor from Typhoon HILS closely matches the electrical characteristics of the real coupled inductor.

On the basis of this observation, the coupled inductors of various coupling factors are implemented by Typhoon HILS and used in the experimental verification of (20) and (21) under buck operation mode. In Fig. 16, the waveforms obtained from multiple coupled inductors of different coupling factors (e.g., 0, −0.2, −0.38, and −0.7) are compared to verify the minimization of inductor current ripple. As shown in Fig. 16, the coupling factor of −0.38 exhibits the smallest ripple size of inductor current.

The ripple size of inductor current versus coupling factor is measured and presented in Fig. 17. For consistent comparison, the measurement is carried out while keeping the duty ratio constant at 0.1, 0.2, 0.3, and 0.4. The curves in Fig. 17 are drawn in accordance with (12), that is, the ripple size of inductor current as a function of coupling factor with the constant parameter of duty ratio. The values of ripple size are displayed in per unit basis with respect to the absolute value at the coupling factor of zero, i.e., non-coupled. The dotted data points in Fig. 17 represent the measurement values from the HILS setup. As shown in Fig. 17, the measurement values from the HILS setup closely follow the pattern of the theoretical curves. Therefore, the theoretical model of (12) is confirmed by the combination of HILS and experiment test. The similar verification of (13) in the range of duty ratio > 0.5 is successfully carried out. The verification result for (13) is omitted in this paper because of space limitations. Fig. 17 shows that, under the duty ratio of 0.4, the minimal inductor current ripple corresponds to the coupling factor of −0.38, which is consistent with the waveforms presented in Fig. 16.

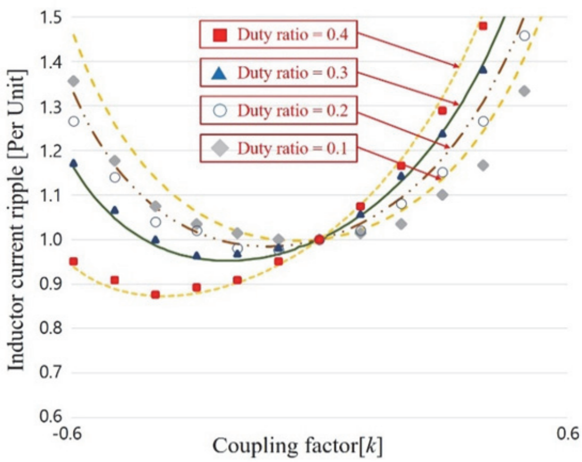

Fig. 17. Mathematical and experimental data of inductor current ripple vs. coupling factor under buck mode and duty < 0.5 [line: mathematical analysis, dot: experiment].

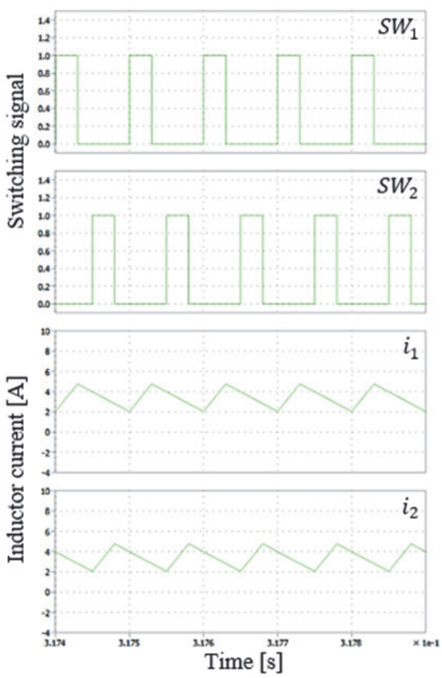

Fig. 18. Simulation waveforms of inductor currents under duty = 0.3 and coupling factor = 0 (non-coupled).

B. Verification of Boost Converter Mode

In this subsection, the simulation and experimental results for the coupled inductor under boost operation mode are presented. Unless otherwise noted in this paper, the simulation and experimental results under boost operation mode correspond to the duty ratio of 0.3. In addition, the simulation and experimental results are compared with a coupling factor of −0.3 (inverse coupling).

Waveforms obtained through the simulation and HILS are presented in Figs. 18 and 19, respectively. The waveforms in these figures correspond to the operation condition under which the duty ratio is set to 0.3 and the coupling factor is

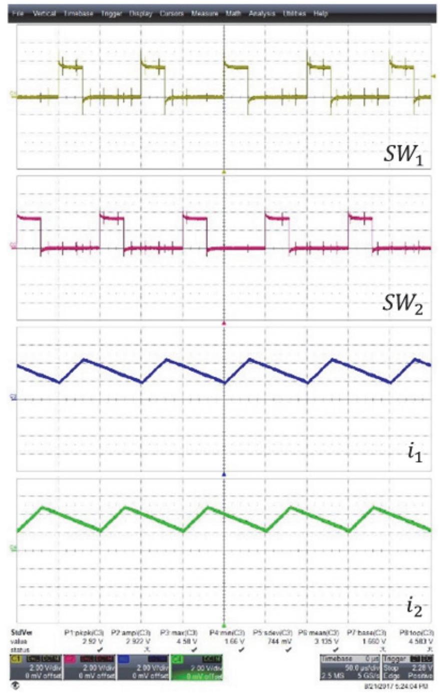

Fig. 19. HILS waveforms of inductor currents under duty = 0.3 and coupling factor = 0 (non-coupled) (i_1, i_2 [2 A/div, 50 us/div]).

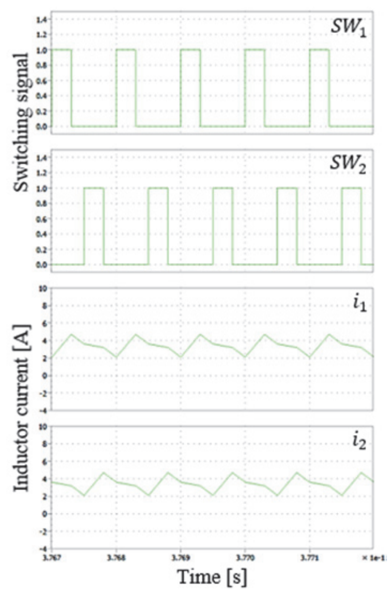

Fig. 20. Simulation waveforms of coupled inductor currents under duty = 0.3 and coupling factor = −0.3.

maintained at 0, i.e., non-coupled. Therefore, these waveforms represent the gate switching signal and the inductor current for the two-phase staggering operation of two boost converter modules with two separate non-coupled inductors. Figs. 20–22 show the simulation, HILS, and experimental waveforms of gate switching signal and the inductor currents (i_1 and i_2) under the duty of 0.3 and the coupling factor of −0.3 (inverse coupling) in the two phase-staggered operation. An obvious contrast is observed between the slope of inductor current in

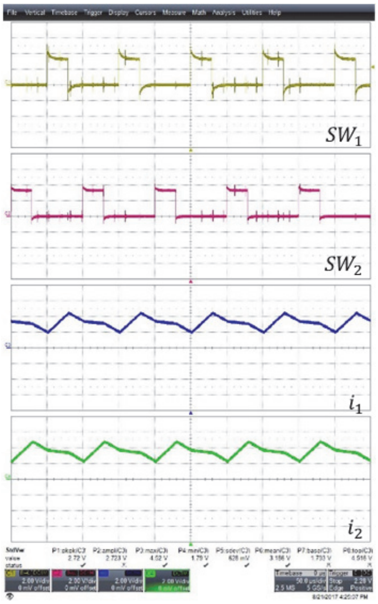

Fig. 21. HILS waveforms of coupled inductor currents under duty = 0.3 and coupling factor = −0.3 (i_1, i_2 [2 A/div, 50 us/div]).

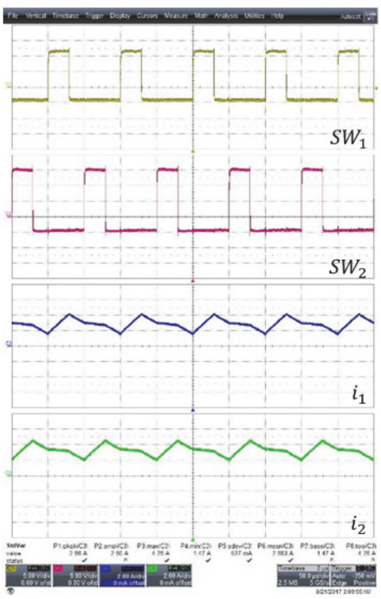

Fig. 22. Experiment waveforms of coupled inductor currents under duty = 0.3 and coupling factor = −0.3 (i_1, i_2 [2A/div, 50 us/div]).

Figs. 18–19 and in Figs. 20–22. Figs. 20–22 show that the magnetic coupling of output inductors leads to the variation in current slope during the ramping down of inductor currents in the same manner as those in Fig. 7.

Fig. 21 shows the waveforms obtained from HILS using the coupled inductor model of Typhoon HILS. The waveforms of inductor current in Fig. 21 are very similar to those in Fig. 22, which were measured from the real experimental setup using the real coupled inductor of the same coupling factor. Therefore, the model of coupled inductor from Typhoon HILS closely matches the electrical characteristics of the real coupled inductor that is also under boost operation mode. On the basis of this observation, the coupled inductors of various coupling factors are implemented by Typhoon HILS and used in the experimental verification of (20) and (21) under boost operation mode. The ripple size of inductor current versus coupling factor is measured and presented in Fig. 23. For consistent comparison, the measurement is carried out while keeping the duty ratio constant at 0.1, 0.2, 0.3, and 0.4. The curves in Fig. 23 are drawn in accordance with (18), that is, the ripple size of inductor current as a function of coupling factor with the constant parameter of duty ratio. The values of ripple size are displayed in per unit basis with respect to the absolute value at the coupling factor of zero, i.e., non-coupled. The dotted data points in Fig. 23 represent the measurement values from the HILS setup. As shown in Fig. 23, the measurement values from the HILS setup closely follow the pattern of the theoretical curves. Therefore, the theoretical model of (18) is confirmed though a combination of the HILS and experiment test. A similar verification of (19) in the range of duty ratio > 0.5 is successfully conducted. The verification result for (19) is omitted in this paper because of space limitations.

The verification results presented in Figs. 11–17 for buck operation mode and Figs. 18–23 for boost operation mode exhibit many similarities. These similarities are due to the same behavior that the theoretical model of (12) and (13) for buck operation mode and the other theoretical model of (18) and (19) for boost operation mode show with respect to the variation in ripple size as a function of coupling factor.

As shown in Figs. 17 and 23, a particular coupling factor value exists at which the ripple size of inductor current becomes minimum. Interestingly, this value for the minimal ripple size is located in the negative side of the coupling factor, i.e., inverse coupling. Therefore, Figs. 17 and 23 indicate that the inverse coupling (negative coupling factor) in limited operation ranges can generate smaller ripple size than the non-coupled case, while direct coupling (positive coupling factor) always provides the largest ripple size. This particular coupling factor value corresponding to a minimal ripple size depends on the value of duty ratio. The optimized coupling factor values with the minimum ripple size of inductor current as a function of duty ratio are plotted in Fig. 24 under buck and boost operation modes. The plotted points in this figure are obtained from Figs. 17 and 23 under buck and boost operation conditions, respectively. These data points from Figs. 17 and 23 match each other well. Thus, buck and boost operation modes generate nearly the same optimized coupling factor values versus duty ratio. This observation is in line with the fact that the theoretical equations of optimal coupling factor, as represented by (20) and (21), are valid for buck and boost operation modes. This fnding is of high practical value in designing the coupled inductor for a bidirectional dc–dc converter because the coupling factor value does not have to be optimized

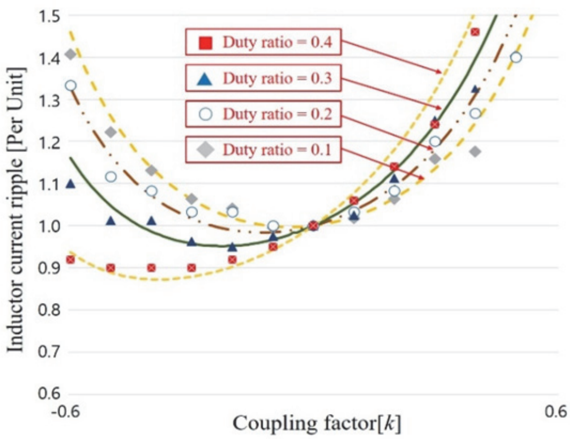

Fig. 23. Mathematical and experimental data of inductor current ripple vs. coupling factor under boost mode and duty < 0.5 [line: mathematical analysis, dot: experiment].

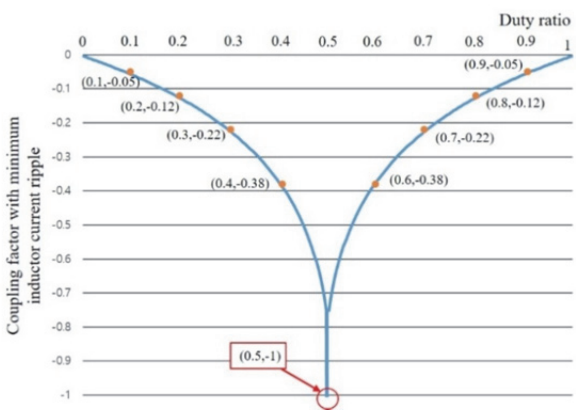

Fig. 24. Coupling factor of the minimum inductor current ripple vs. duty ratio [line: mathematical analysis, dot: experiment] [Buck mode and Boost mode].

separately for buck and boost operation modes. In other words, once the coupled inductor is optimized for either buck or boost operation mode, then it also becomes optimized for the other operation mode in a bidirectional dc–dc converter. The experimental data presented in Fig. 24 clearly prove this theoretical argument for (20) and (21).

Fig. 24 shows that, as duty ratio approaches 0.5, the optimal coupling factor value becomes −1, i.e., inverse coupling without leakage inductances. On the contrary, when the operation points for the duty ratio move to 0 or 1, the optimal coupling factor value becomes 0, i.e., zero mutual inductance (L_m). The optimized coupling factor values of (20) and (21), which correspond to a minimal ripple size of inductor current under buck and boost operation modes, can be a useful engineering guideline for practical engineers when designing coupled inductors applied in bidirectional dc–dc converters.

Table IV shows the power loss data of conduction, switching-on, and switching-off loss factor. As shown in the table, the conduction and switching-off loss factors are

TABLE IV
COMPARISON OF SWTICH POWER LOSSES UNDER NON-COUPLED AND COUPLED CASES

	$P_{Cond.}$	$P_{SWon.}$	P_{SWoff}	P_{total}
Non-coupled ($k = 0$)	3.66 W	0.29 W	3.51 W	7.46 W
Coupled ($k = -0.3$)	3.60 W	0.52 W	3.32 W	7.44 W

decreased by employing the coupled inductor compared with those by using the non-coupled inductor. In conclusion, the total loss value for the switching device decreases by 0.25% compared with that for the non-coupled case. Although the improvement is insignificant, the coupling of inductors may contribute better than the loss factor of inductor and the required maximum current rating of power semiconductor devices, especially in high-power applications.

V. CONCLUSION

A half-bridge bidirectional dc–dc converter is a commonly used power converter topology in a power conditioning system of BESS. The output/input coupled inductor plays a significant role in determining many important electrical characteristics of BESS, such as the ripple size of battery charging/discharging current, harmonic contents in input/output current, and peak current stress on power semiconductor switches.

This study proposes a simple and unique design guideline for optimal coupling factor of the coupled inductor to minimize the peak-to-peak ripple of inductor current. Compared with previous works, this study investigates this novel guideline for buck and boost operation modes of bidirectional converters. Results show that the optimal coupling factor values corresponding to a minimal ripple size of inductor current exhibit the same distribution pattern under buck and boost operation modes. This finding is important from a practical point of view because most bidirectional converters use a single coupled inductor that is subject to buck and boost operation modes, i.e., a bidirectional power flow. As a result, once the coupled inductor is equipped with an optimized coupling factor value, the inductor generates a minimal inductor current ripple under buck and boost operation modes. This argument is confirmed through simulation and experimental results with the help of the HILS model of the coupled inductor. This new engineering argument will greatly help industry engineers in designing coupled inductors for bidirectional dc–dc converters.

ACKNOWLEDGMENT

This research was supported by Korea Electric Power Corporation (Grant number : R18XA04) and the research funds of Chonbuk National University in 2015.

REFERENCES

[1] A. S. Subburaj, W. B. Ray, and S. B. Bayne, "Comparison study of the controllers for grid connected battery system," in *IEEE NewNEB DC Utility Power Conference and Exhibition*, pp. 1-6, 2014.

[2] F. Lin, H. Chiang, J. Chang, and Y. Chang, "Intelligent wind power smoothing control with BESS," *IET Renew. Power Gener.*, Vol. 11, No. 2, pp. 398-407, Aug. 2017.

[3] J. Philip, C. Jain, K. Kant, B. Sigh, S. Mishra, A. Chandra, and K. Ai-haddad, "Control and implementation of standalone solar photovoltaic hybrid system." in *IEEE Trans. Ind. Appl.*, Vol. 52, No. 4, pp. 3472-3479, Jul. 2016.

[4] M. Farrokhabadi, S. Koenig, C. A. Canizares, K. Bhattacharya, and T. Leibfried, "Battery energy storage system model for microgrid stability analysis and dynamic simulation," *IEEE Trans. Power Syst.*, Vol. 33, No. 2, pp. 2301-2312, Mar. 2018.

[5] Z. Guo, K. Sun, T. Wu, and C. Li, "An improved modulation scheme of current-fed bi-directional DC-DC converters for loss reduction," *IEEE Trans. Power Electron.*, to be published.

[6] I. Song, D. Jung, Y. Ji, S. Choi, S. Lee, and C. Won, "A residential 10kWh lithium-polymer battery energy storage system," in *8th International Conference on Power Electrics-ECCE Asia*, pp. 2625-2630, 2011.

[7] H. Sangtaek and D. Divan, "Bi-directional dc/dc converters for plug-in hybrid electric vehicle (PHEV) applications," in *IEEE 2008 Applied Power Electronics Conference and Exposition*, pp. 784-789, 2008.

[8] K. W. Klontz, A. Esser, P. J. Wolfs, and D. M. Divan, "Converter selection for electric vehicle charger systems with a high-frequency high-power link," in *IEEE 1993 Power Electronics Specialists Conference*, pp. 855-861, 1993.

[9] D. Pavkovic, Mihael C, M. Hrgetic, A. Komljenovic, and V. Smetko, "Battery current and voltage control system design with charging application," in *IEEE Conference on control application(CCA)*, pp. 1133-1138, 2014.

[10] J. Czogalla, J. Li, and C. R. Sullivan, "Automotive application of multi-phase coupled-inductor dc-dc converter," in *IEEE Industry Applications Conference,* Vol. 3, pp. 1524-1529, 2003.

[11] L. Ni, D. J. Patterson, and J. L. Hudgins "High power current sensorless bidirectional 16-phase interleaved DC-DC converter for hybrid vehicle application," *IEEE Trans. Power Electron.*, Vol. 27, No. 3, pp. 1141-1151, Mar. 2012.

[12] G. Zhu, B. A. McDonald, and K. Wang, "Modeling and analysis of coupled inductors in power converters," *IEEE Trans. Power Electron.*, Vol. 26, No. 5, pp, 1355-1363, May 2011.

[13] J. Imaoka, Y. Ishikura, T. Kawashima, and M. Yamamoto, "Optimal design method for interleaved single-phase PFC converter with coupled inductor," in *IEEE Energy Conversion Congress and Exposition*, pp. 1807-1812, 2011.

[14] J. Imaoka, M. Yamamoto, K. Umetani, and S. Arimura, "Characteristics analysis and performance evaluation for interleaved boost converter with integrated winding coupled inductor," in *Energy Conversion Congress and Exposition*, pp. 3711-3718, 2013.

[15] S. Lu, M. Mu, Y. Jiao, F. C. Lee, and Z. Zhao, "Coupled inductors in interleaved multiphase three-level DC–DC converter for high-Power applications," *IEEE Trans. Power Electron.*, Vol. 31, No. 1, pp. 120-134, Jan. 2016.

[16] H. N. Nagaraja, D. Kastha, and A. Petra, "Design principles of a symmetrically coupled inductor structure for multiphase synchronous buck converters," *IEEE Trans. Power Electron.*, Vol. 58, No. 3, pp. 988-997, Mar. 2011.

[17] B. C. Barry, J. G. Hayes, and M. S. Ryłko, "CCM and DCM operation of the interleaved two-phase boost converter with discrete and coupled inductors," *IEEE Trans. Power Electron.*, Vol. 30, No. 12, pp. 6551-6567, Dec. 2015.

[18] Y. Yang, J. Ma, C. N. Ho, and Y. Zou, "A new coupled-inductor structure for interleaving bidirectional DC-DC converters," *IEEE J. Emerg. Sel. Topics Power Electron.*, Vol. 3, No. 3, pp. 841-849, Sep. 2015.

[19] T. Kang, Y. Suh, H. Park, B. Kang, and S. Kim, "A design and control of rapid electric vehicle charging system for lithium-ion battery," *Trans. Korean Inst. Power Electron. (KIPE)*, Vol. 18, No. 1, pp. 26-36, Feb. 2013.

[20] T. Kang, B. Chae, and Y. Suh "Control algorithm of bi-directional power flow rapid charging system for electric vehicle using Li-Ion polymer battery" in *2013 ECCE Asia Downunder*, pp. 499-505, 2013.

[21] T. Kang, B. Chae, T. Kang, and Y. Suh "Design of coupled inductor for minimum inductor current ripple in rapid traction battery charger systems" in *IEEE Energy Conversion Congress and Exposition (ECCE)*, pp. 358-364, 2014.

[22] T. Kang, and Y. Suh, "Design of optimized coupling factor for minimum inductor current ripple in rapid EV charger systems using multi-winding coupled inductor," in *IEEE Energy Conversion Congress and Exposition (ECCE)*, pp. 5667-5674, 2015

[23] P-L. Wong, P. Xu, B. Yang, and F. C. Lee, "Performance improvements of interleaving VRMs with coupling inductors," *IEEE Trans. Power Electron.*, Vol. 16, No. 4, pp. 499-507, Jul. 2001.

[24] L. Chen "Design of duty-varied voltage pulse charger for improving Li-Ion battery-charging response," *IEEE Trans. Ind. Electron.*, Vol. 56, No. 2, pp. 480-486, Feb. 2009.

[25] M. Jung, "Optimized design DC-DC converter LC output filter for EV battery charging applications in terms of defined battery current and voltage ripple as well as overall efficiency," in *EPE.16 ECCE Europe*, pp.1-8, 2016.

[26] M. N. Hussain and V. Agrarwal, "A new control technique to enhance the stability of a DC microgrid and to reduce battery current ripple during the charging plug-in-electric vehicle," in *2015 IEEE 15th International Conference on Environment and Electrical Engineering*, pp. 2189-2193, 2015.

[27] R. S. Kumar, K. S. Kumar, and M. K. Mishra, "Dynamic energy management of micro grids using battery super capacitor combined storage," in *Proc. 2012 Annual IEEE India Conference (INDICON)*, pp. 1078-1083, 2012.

[28] K. Kroics, J. Zakis, and U. Sirmelis, "Multi phase interleaved DC-DC converter with directly and inversely coupled inductors," in *57th International Scientific Conference on Power and Electrical Engineering of RIGA Technical University*, pp. 1-6, 2016.

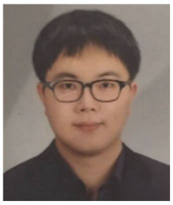

Taewon Kang was born in Jeonju, Korea. He received his B.S. and M.S. degrees in Electronics Engineering from Chonbuk National University, Jeonju, Korea, in 2004 and 2013, respectively. Since 2013, he has been pursuing his Ph.D. in Power Electronic Engineering at the Environmental Friendly Energy Conversion Laboratory in Chonbuk National University, Jeonju, Korea, under the supervision of Professor Yongsug Suh. His current research interests include design of coupled inductor, design of power stage, and traction battery charging system for electric vehicles.

Yongsug Suh was born in Seoul, Korea. He received his B.E.E. and M.S.E.E. degrees from Yonsei University, Seoul, Korea, in 1991 and 1993, respectively; and his Ph.D. degree in Electrical Engineering from the University of Wisconsin, Madison, in 2004. From 1993 to 1998, he was an application engineer in the Power Semiconductor Division of Samsung Electronics Co. From 2004 to 2008, he was a senior engineer in the Power Electronics & Medium-Voltage Drives Division of ABB, Turgi, Switzerland. Since 2008, he has been with the Department of Electrical Engineering, Chonbuk National University, Jeonju, Korea, where he is currently a professor. His research interests include power conversion systems of high power for renewable energy sources and electric drive systems of medium voltage.